SUPPLEMENTARY MATERIAL

Crystallographic Tomography and Molecular Modelling of Structured Organic Polycrystalline Powders

P. Gajjar[a], T. T. H. Nguyen[b], J. Sun[c], I. D. Styliari[d], H. Bale[e], S. A. McDonald[a], T. Burnett[a], B. Tordoff[f], E. Lauridsen[c], R. B. Hammond[b], D. Murnane[d], P. J. Withers[a,g], and K. Roberts[b]

[a]Henry Moseley X-ray Imaging Facility, Department of Materials, The University of Manchester, Manchester, M13 9PL, UK
[b]Centre for the Digital Design of Drug Products, School of Chemical and Process Engineering, University of Leeds, Woodhouse Lane, Leeds, LS2 9JT, UK
[c]Carl Zeiss X-ray Microscopy, 4385 Hopyard Rd #100, Pleasanton, CA 94588, USA
[d]School of Life and Medical Sciences, University of Hertfordshire, College Lane, Hatfield, AL10 9AB, UK
[e]Xnovo Technology ApS, Theilgaards Alle 9,1th., 4600 Køge Denmark
[f]Carl Zeiss Microscopy GmbH, Carl-Zeiss-Straße 22, 73447 Oberkochen, Germany
[g]Henry Royce Institute for Advanced Materials, The University of Manchester, Manchester, M13 9PL, UK

1 Laboratory Diffraction Contrast Tomography (LabDCT)

In a traditional attenuation based X-ray CT setup, an x-ray beam is incident on the sample, with the sample absorbing some photons as the x-rays pass through it. The transmitted beam recorded on a detector giving a projection image. By mathematically reconstructing a number of projections taken about a 360° rotation of the sample, a virtual volume representation of the sample is formed which can be analysed to reveal internal structure (Feldkamp et al., 1984), including features such as cracks or defects (Lu et al., 2018). The deployment of x-ray optics has led to instruments with greater contrast and improved resolution (Lavery et al., 2014) that have provided valuable insight into a range of materials incldluing soft biological structures (Shearer et al., 2016), polymer particles (Gamble et al., 2016) and parasitic behaviour (O'Sullivan et al., 2018). Diffraction Contrast Tomography additionally incorporates diffraction data to provide crystallographic analysis of the sample. Overall, DCT involves three main steps. Firstly an attenuation X-ray CT scan is acquired in the same manner as above. Secondly, a DCT scan is performed, with a tungsten aperture placed between the source and sample to centralise the beam, and a tungsten beam stop between the sample and detector to prevent stronger transmitting x-rays from flooding the detector, as shown in figure 1. The source-to-sample and sample-to-detector distances are kept equal to obey the Laue condition, which focuses the diffracted beam onto the detector in line-shaped spots, increases the signal to noise ratio and substantially reduces overlap between different diffraction spots. Diffraction images are recorded as the sample is rotated through 360°. Finally, the known crystal lattice parameters are used with the absorption and diffraction datasets to search for all possible crystal position-orientation combinations, and identify those with the highest confidence. Readers interested in the physics behind DCT are directed to McDonald et al. (2015), Holzner et al. (2016) and Bachmann et al. (2019). Whilst DCT was first implemented on synchrotron beamlines (Ludwig et al., 2010; Lienert et al., 2011; Reischig et al., 2013), the integration of DCT modules within laboratory-based XRM systems has made DCT an accessible laboratory technique (labDCT) (McDonald et al., 2015; Feser et al., 2015) that can provide information on grain centroids and orientations, grain shape and grain boundary networks. A photograph of the prepared hexamine sample is shown in Figure 2a, with examples of attenuation X-ray CT and diffraction projections shown in Figure 2b,c.

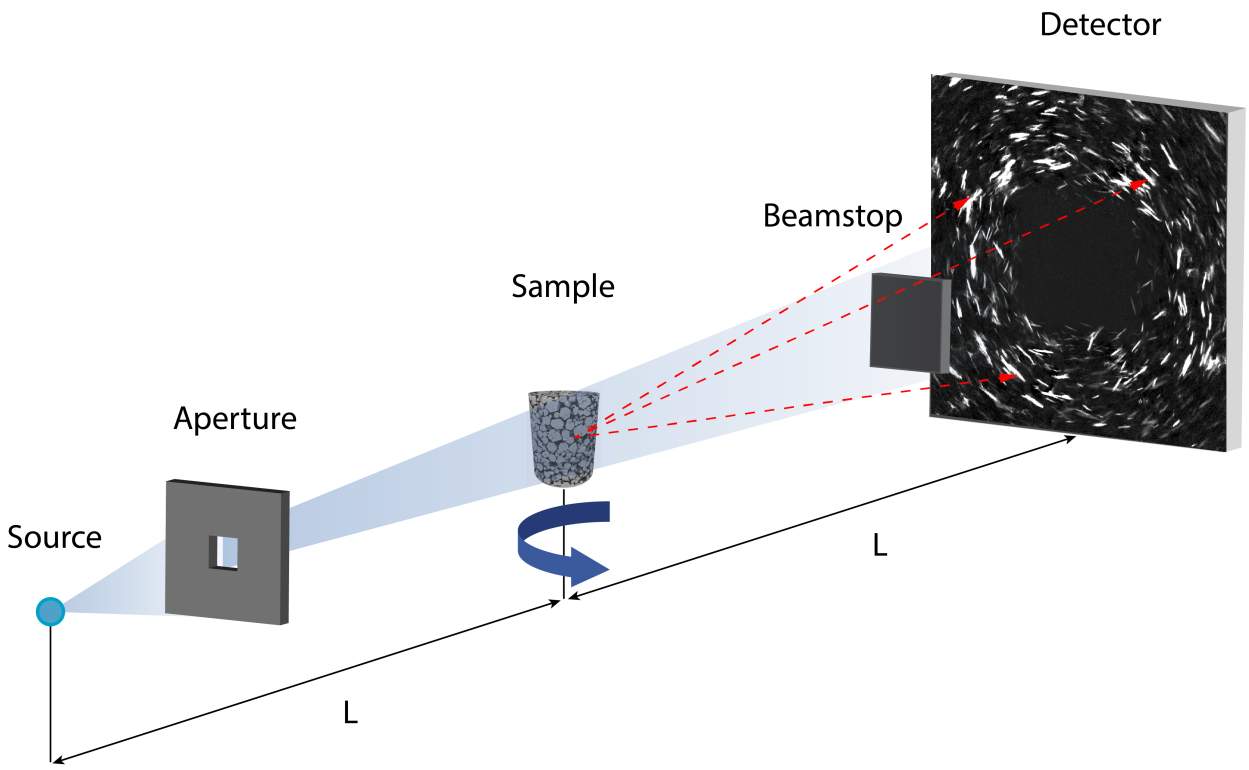

Figure 1 The experimental DCT setup, modified from a traditional X-ray CT setup through an aperture and beamstop. Both the source and detector are an equal distance L from the sample to obey the Laue focusing condition, giving line-like spots in the diffraction imageBachmann et al. (2019).

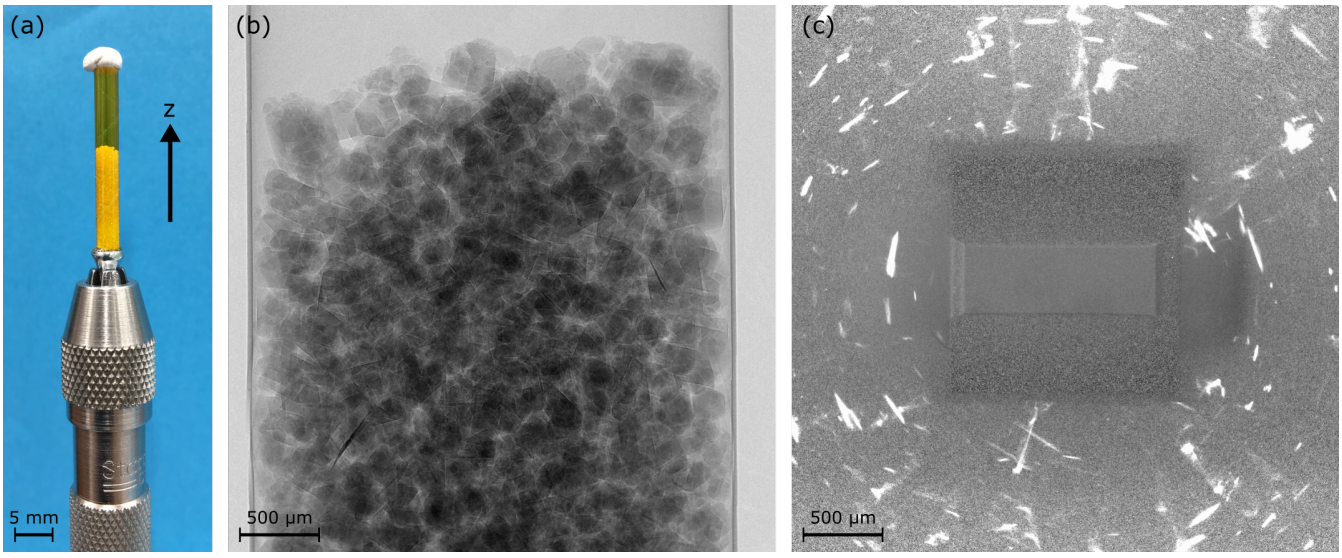

Figure 2 (a) Hexamine crystal powder bed within polyimide tubing; (b) An absorption projection image showing the powder bed; (c) A single labDCT diffraction projection image showing the line-like diffraction spots.

2 Modelling Hexamine Crystal Morphology

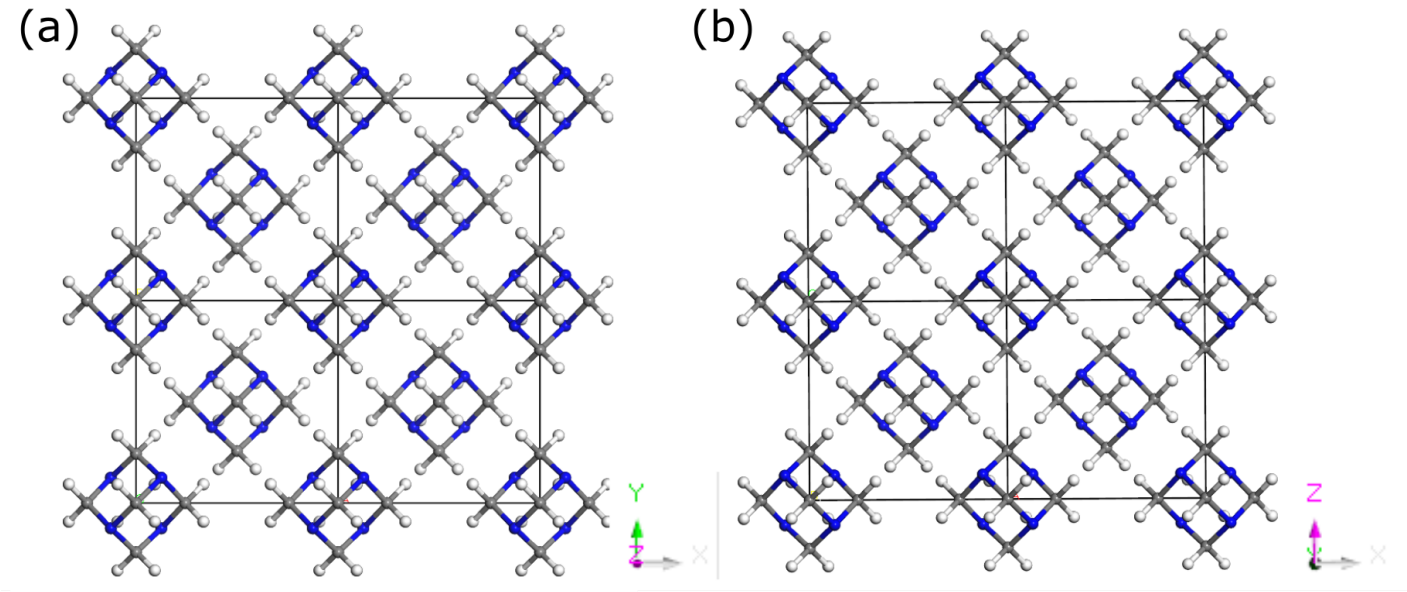

Figure 3 Molecular packing of hexamine (a) looking along the ¡001¿ direction; (b) looking along the ¡010¿ direction.

The packing of molecules within a Hexamine unit cell is shown in Figure 3, highlighting the body-centered cubic nature.

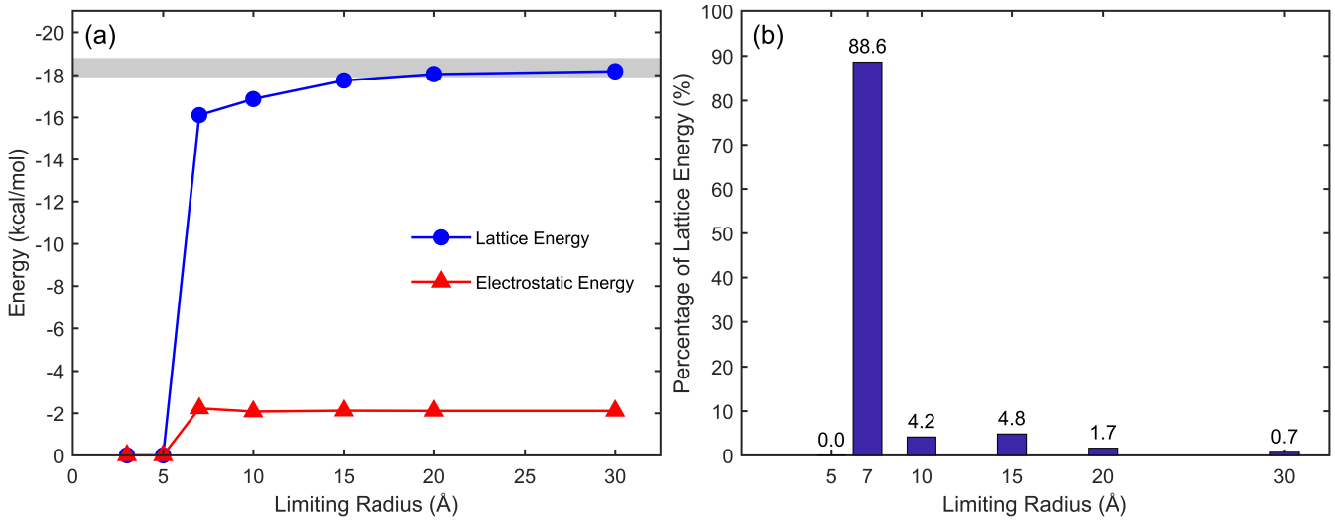

Figure 4 (a) Lattice energy E_{cr} as a function of increasing limiting radius of the sphere of calculation using the Dreiding set. Range of experimental sublimation enthalpy ΔH_{sub} measurements is shown shaded in grey for comparison. (b) the % of the lattice energy added with an increase in the radius of the sphere using the Dreiding II potential set.

The lattice energy convergence as a function of limiting radius of the calculation is shown in Figure 4a. The calculated lattice energy E_{cr} using the Dreiding potential set converged to $-18.18\,\mathrm{kcal/mol}$, which has good agreement with the experimental lattice energy calculated from the heat of sublimation ΔH_{sub} summarized in Table 1. This suggests that the Dreiding potential provides an acceptable reproduction of the strength and nature of the synthons within the crystal structure for hexamine. Figure 4a also shows that the electrostatic interactions contributed a relatively small amount to the lattice energy, without contributions from hydrogen bonds, reflecting that the majority of the molecule is apolar in nature.

Table 1 Experimental sublimation enthalpies (ΔH_{sub}) for hexamine crystals from the literature. For comparison, the calculated lattice energy E_{latt} is $-18.18\,\mathrm{kcal/mol}$.

ΔH_{sub} (kcal/mol)	T_{melt} (K)	Reference
17.9 ± 0.7	298	Wada et al. (1960)
18.8	316	De Wit et al. (1983)
18.4	313	Stephenson and Malanowski (1987)

Figure 4b shows the addition of energy as more molecules are added to the crystal structure as the limiting radius is increased, with respect to the origin molecule. This is shown as a column graph with each column representing the percentage of the energy added at that step; i.e., the column at $10\,$Å is the amount of energy added with the increase between 7 and $10\,$Å of the radius of the sphere.

3 Powder Bed Structure

The size-distribution statistics for the powder bed are provided in Table 2. The particle size data from attenuation X-ray CT shows a wide range of sizes, indicative of the highly agglomerated nature of the powder bed. The crystallite size-distribution from DCT has a much narrower range of sizes, and matches the particle size data filtered less than $< 300\,\mu$m.

Table 2 Size distribution of the hexamine powder bed measured from attenuation X-ray CT and DCT. All measurements in microns.

	D10	D50	D90
Particle size distribution	225	495	1069
Crystallite size distribution	105	210	258
Size distribution of particles $< 300\,\mu$m	116	215	261

4 Crystal Interactions

Table 3 provides the crystallographic information from DCT measurements used to reconstruct models of the interacting crystallites.

Table 3 A summary of the experimental information for the crystal clusters in Figure 10 of the main article for creating the model crystal interactions.

Crystal	Equivalent Diameter (μm)	Reference crystal	Transformation to reference crystal co-ordinate system		
			Rotation Axis	Rotation Angle	Translation (μm)
G_1	164	G_1	n/a	n/a	n/a
G_2	105	G_1	[-0.68,-0.72,0.11]	66.4°	[-28.9,-106.6,-15.4]
G_3	228	G_1	[0.06,-0.46,0.89]	1.4°	[-120.8,5.5,-76.3]
I_1	271	I_1	n/a	n/a	n/a
I_2	264	I_1	[0.33,0.89,-0.32]	65.8°	[10.8,159.0,179.8]
J_1	229	J_1	n/a	n/a	n/a
J_2	305	J_1	[0.58,0.59,0.57]	60.1°	[15.3,183.7,-138.0]
J_3	223	J_1	[0.39,0.73,0.56]	47.3°	[240.3,209.1,-79.0]

References

F. Bachmann, H. Bale, N. Gueninchault, C. Holzner, and E. M. Lauridsen. 3D grain reconstruction from laboratory diffraction contrast tomography. *Journal of Applied Crystallography*, 52(3):643–651, Jun 2019. doi: 10.1107/S1600576719005442. URL https://doi.org/10.1107/S1600576719005442.

H. G. M. De Wit, J. C. Van Miltenburg, and C. G. De Kruif. Thermodynamic properties of molecular organic crystals containing nitrogen, oxygen, and sulphur 1. vapour pressures and enthalpies of sublimation. *The Journal of Chemical Thermodynamics*, 15(7):651–663, July 1983. ISSN 0021-9614. URL http://www.sciencedirect.com/science/article/pii/0021961483900794.

L. A. Feldkamp, L. C. Davis, and J. W. Kress. Practical cone-beam algorithm. *Journal of the Optical Society of America A, Optics and Image Science*, 1(6):612–619, Jun 1984. doi: 10.1364/JOSAA.1.000612.

M. Feser, C. Holzner, and E. M. Lauridsen. Laboratory x-ray micro-tomography system with crystallographic grain orientation mapping capabilities, 2015. URL https://patents.google.com/patent/US9110004.

J. F. Gamble, M. Terada, C. Holzner, L. Lavery, S. J. Nicholson, P. Timmins, and M. Tobyn. Application of x-ray microtomography for the characterisation of hollow polymer-stabilised spray dried amorphous dispersion particles. *International Journal of Pharmaceutics*, 510(1):1–8, Aug. 2016. ISSN 0378-5173. URL http://www.sciencedirect.com/science/article/pii/S0378517316304409.

C. Holzner, L. Lavery, H. Bale, A. Merkle, S. McDonald, P. Withers, Y. Zhang, D. J. Jensen, M. Kimura, A. Lyckegaard, P. Reischig, and E. M. Lauridsen. Diffraction contrast tomography in the laboratory - applications and future directions. *Microscopy Today*, 24(4):34–43, 2016. ISSN 1551-9295. doi: 10.1017/s1551929516000584. URL https://www.cambridge.org/core/article/diffraction-contrast-tomography-in-the-laboratory-applications-and-future-directions/955B1809FFAB0C73F0B2CD325E396891.

L. L. Lavery, J. Gelb, A. P. Merkle, and A. Steinbach. X-ray microscopy for hierarchical multi-scale materials. *Microscopy Today*, 22(3):16–21, 2014. doi: 10.1017/S155192951400056X.

U. Lienert, S. F. Li, C. M. Hefferan, J. Lind, R. M. Suter, J. V. Bernier, N. R. Barton, M. C. Brandes, M. J. Mills, M. P. Miller, B. Jakobsen, and W. Pantleon. High-energy diffraction microscopy at the advanced photon source. *JOM Journal of the Minerals Metals and Materials Society*, 63(7):70–77, July 2011. ISSN 1543-1851. URL https://doi.org/10.1007/s11837-011-0116-0.

X. Lu, S. D. Rawson, and P. J. Withers. Effect of hydration and crack orientation on crack-tip strain, crack opening displacement and crack-tip shielding in elephant dentin. *Dental Materials*, 34(7):1041–1053, July 2018. ISSN 0109-5641. URL http://www.sciencedirect.com/science/article/pii/S0109564117310904.

W. Ludwig, A. King, M. Herbig, P. Reischig, J. Marrow, L. Babout, E. M. Lauridsen, H. Proudhon, and J. Y. Buffière. Characterization of polycrystalline materials using synchrotron x-ray imaging and diffraction techniques. *JOM Journal of the Minerals Metals and Materials Society*, 62(12):22–28, Dec. 2010. ISSN 1543-1851. URL https://doi.org/10.1007/s11837-010-0176-6.

S. A. McDonald, P. Reischig, C. Holzner, E. M. Lauridsen, P. J. Withers, A. P. Merkle, and M. Feser. Non-destructive mapping of grain orientations in 3D by laboratory X-ray microscopy. *Scientific Reports*, 5(1):14665, Oct. 2015. ISSN 2045-2322. URL https://doi.org/10.1038/srep14665.

J. D. B. O'Sullivan, J. Behnsen, T. Starborg, A. S. MacDonald, A. T. Phythian-Adams, K. J. Else, S. M. Cruickshank, and P. J. Withers. X-ray micro-computed tomography (μCT): an emerging opportunity in parasite imaging. *Parasitology*, 145(7):848–854, 2018. ISSN 0031-1820. doi: 10.1017/s0031182017002074. URL https://www.cambridge.org/core/article/xray-microcomputed-tomography-ct-an-emerging-opportunity-in-parasite-imaging/DCCF076094EE48CFEC9855992435D31E.

P. Reischig, A. King, L. Nervo, N. Viganó, Y. Guilhem, W. J. Palenstijn, K. J. Batenburg, M. Preuss, and W. Ludwig. Advances in X-ray diffraction contrast tomography: flexibility in the setup geometry and application to multiphase materials. *Journal of Applied Crystallography*, 46(2):297–311, Apr 2013. doi: 10.1107/S0021889813002604. URL https://doi.org/10.1107/S0021889813002604.

T. Shearer, R. S. Bradley, L. A. Hidalgo-Bastida, M. J. Sherratt, and S. H. Cartmell. Three-dimensional visualisation of soft biological structures by X-ray computed micro-tomography. *Journal of Cell Science*, 129(13):2483, July 2016. URL http://jcs.biologists.org/content/129/13/2483.abstract.

R. M. Stephenson and S. Malanowski. Properties of organic compounds. In R. M. Stephenson and S. Malanowski, editors, *Handbook of the Thermodynamics of Organic Compounds*, pages 1–471. Springer Netherlands, Dordrecht, 1987. URL https://doi.org/10.1007/978-94-009-3173-2_1.

T. Wada, E. Kishida, Y. Tomiie, H. Suga, S. Seki, and I. Nitta. Crystal Structure and Thermodynamical Investigations of Triethylenediamine, C6H12N2. *Bulletin of the Chemical Society of Japan*, 33(9):1317–1318, 1960. doi: 10.1246/bcsj.33.1317. URL https://doi.org/10.1246/bcsj.33.1317.